

# Theory of particle beams transport over curved plasma-discharge capillaries

A. Frazzitta<sup>1</sup>, R. Pompili<sup>2</sup>, and A. R. Rossi<sup>3</sup>

<sup>1</sup>University of Rome Sapienza, Piazzale Aldo Moro 5, 00185 Rome, Italy

<sup>2</sup>Laboratori Nazionali di Frascati, Via Enrico Fermi 54, 00044 Frascati, Italy

<sup>3</sup>INFN Milano, via Celoria 16, 20133 Milan, Italy

 (Received 7 May 2024; accepted 20 August 2024; published 13 September 2024)

We present a new approach that demonstrates the deflection and guiding of relativistic electron beams over curved paths by means of the magnetic field generated in a plasma-discharge capillary. The active bending plasma (ABP) represents a promising solution that has been recently demonstrated with a proof of principle experiment. An ABP device consists of a curved capillary where large discharges (of the order of kA) are propagated in a plasma channel. Unlike conventional bending magnets, in which the field is constant over the bending plane, in the ABP, the azimuthal magnetic field generated by the discharge grows with the distance from the capillary axis. This feature makes the device less affected by the beam chromatic dispersion so that it can be used to efficiently guide particle beams with non-negligible energy spreads. The study we present in the following aims to provide a theoretical basis of the main ABP features by presenting an analytical description of a single-particle motion and rms beam dynamics. The retrieved relationships are verified by means of numerical simulations and provide the theoretical matrix formalism needed to completely characterize such a new transport device.

DOI: [10.1103/PhysRevAccelBeams.27.091301](https://doi.org/10.1103/PhysRevAccelBeams.27.091301)

## I. INTRODUCTION

The idea to use curved plasma capillaries is not new in the literature and has been employed to successfully guide laser pulses over nonstraight paths [1–3]. So far, however, their use was never exploited to guide and bend charged particle beams. Indeed, while the straight version (active plasma lens, APL) has been discussed in several articles [4–6], the curved one was introduced few years ago [7] and its demonstration was provided only very recently with a proof of principle experiment [8]. Its theoretical formalism, however, was not yet provided and represents the goal of the present work, providing equations for the proper transport conditions.

The idea behind the ABP is rather simple: (i) an inert gas is injected into a cylindrical-section capillary whose axis describes an arc of a circle; (ii) two electrodes placed at the capillary tips ionize the gas through a discharge at several kV; and (iii) the current density generates an azimuthal magnetic field centered on the capillary axis and with a magnitude that increases with distance. By injecting the beam at the correct position relative to the axis, it is possible to satisfy the beam rigidity equation and curve its trajectory. The effect of the radially increasing field in both the

bending and transverse planes is to achieve intense focusing in both directions. The high magnetic field gradients allow to bend ultrarelativistic beams over short distances: as an example, from the results shown in Sec. II, it can be observed that a 2 mm radius capillary with  $\approx 5$  kA discharge-current is able to bend a 1 GeV electron beam with an equivalent 2 m bending radius. In general, the device can reach high peak fields, comparable to the most high-performing conventional magnets and provide high focusing field gradients along the two transverse planes.

This paper aims to provide the theoretical background describing the ABP working principle. In Sec. II, the transfer matrix of the device is obtained and discussed similar to the cyclotron case. Here, several considerations regarding dispersion also show the main differences with respect to a CBM from the beam dynamics point of view. The matching conditions are retrieved by solving the envelope equation in cylindrical coordinates. We also introduce the effects on the dynamics arising from nonlinear effects. A parametric scan on the beam emittance, spot, and duration is also performed and discussed. Finally, in Sec. III, we show a comparison between the analytical expressions and the numerical simulations of the ABP.

## II. ABP SINGLE PARTICLE AND BEAM DYNAMICS

The focusing field produced by the active plasma lens strongly depends on the discharge dynamics along the

---

Published by the American Physical Society under the terms of the [Creative Commons Attribution 4.0 International license](https://creativecommons.org/licenses/by/4.0/). Further distribution of this work must maintain attribution to the author(s) and the published article's title, journal citation, and DOI.

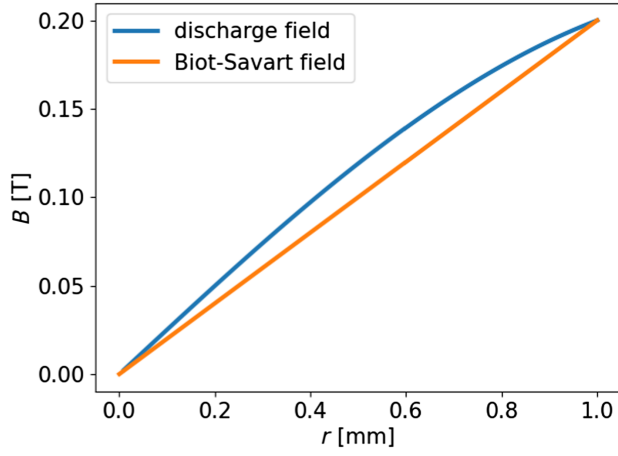


FIG. 1. ABP magnetic field: field amplitude as a function of distance from the axis of the capillary: comparison between a realistic discharge field [10] (blue) and the current-equivalent Biot-Savart type field (orange). Note that the discharge field tends to a linear behavior near capillary axis.

capillary. To describe the main effects of the capillary discharge process, we followed a one-dimensional analytical model that gives expressions for equilibrium plasma temperature and density as a function of radial position [9]. The balance between Ohmic heating and cooling due to the electron heat conduction results in an electric conductivity expression that gives a cosinelike current density profile. Ampere law then provides a nonlinear azimuthal magnetic field, with a steeper trend near capillary axis. In Fig. 1, a plot of the nonlinear field and the Biot-Savart field equivalent to the total current can be observed. In the following section, the equations will be developed using the linear Biot-Savart field for simplicity. The obtained results are scalable to reproduce the slope of the real field, which shows linear behavior near the axis.

### A. Equilibrium radius and lower limit current

Joining case-suited Biot-Savart law  $B = B'(\rho - \rho_c) = \mu_0 I(\rho - \rho_c)/2\pi r_c^2$  and the beam rigidity equation  $B\rho = p/q$ , an equation for the equilibrium radius is found

$$B'\rho^2 - B'\rho_c\rho - \frac{\gamma mc}{q} = 0, \quad (1)$$

whose solution is

$$\rho_0 = \frac{\rho_c}{2} \left( 1 + \sqrt{1 + \frac{8\pi mc r_c^2 \gamma}{\mu_0 q \rho_c^2 I}} \right) \approx \rho_c + \tilde{I}_0 \frac{r_c^2 \gamma}{\rho_c I}, \quad (2)$$

where  $\rho$  denotes the radial coordinate,  $\rho_c$  is the radius of curvature of the capillary axis,  $\mu_0$  the magnetic permeability of vacuum,  $I$  the current in the capillary,  $r_c$  denotes the inner radius of the capillary's circular cross section [see Figs. 2(a) and 2(b)],  $B'$  stands for  $dB/d\rho$ ,  $p \approx \gamma mc$  denotes

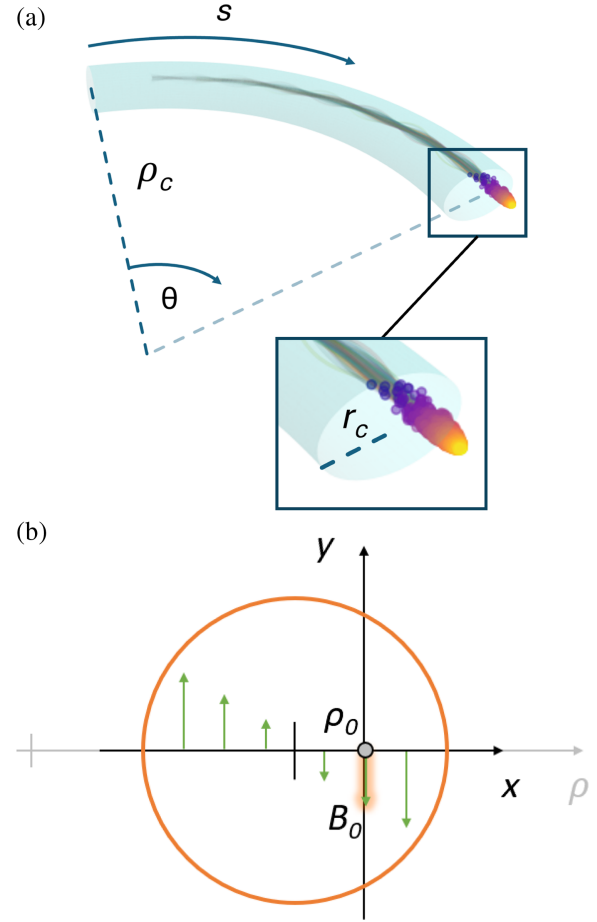


FIG. 2. ABP reference system: (a) capillary render and coordinates:  $\rho_c$ , bending radius;  $r_c$ , capillary section radius;  $s$ , curvilinear coordinate along the capillary axis; and  $\theta$ , bending angle. In orange, a sketch of the ABP bent capillary with a detail on transverse section. (b) Beam particle coordinates represented on capillary transverse section: Cartesian reference system  $(x, y)$  with origin centered on the beam mean equilibrium radius  $\rho_0$ , associated with the magnetic field  $B_0$  satisfying the beam rigidity equation. In orange, capillary circular inner boundary.

the mean beam particles' momentum magnitude, and  $q$  denotes the particle's charge,  $\tilde{I}_0 = I_0/2 = 2\pi mc/\mu_0 q$  represents half of the charged particle's characteristic current,  $\gamma = (1 - \beta^2)^{-1/2}$  ( $\beta = v/c$  being the normalized average beam velocity) represents the average Lorentz factor of the beam,  $m$  is the particle's mass, and  $c$  the speed of light. The approximation in Eq. (2) is valid when  $r_c/\rho_c \ll 1$ . To ensure a real solution in Eq. (2),  $\text{sign}(q) = \text{sign}(I)$  is needed: this means that an electron beam ( $q = -e$ ) will require  $I < 0$ , i.e., the plasma electrons must flow in the same direction as the beam electrons. As expected, the equilibrium radius defined in Eq. (2) is proportional to the energy of the beam and inversely proportional to the current. From Eq. (2), the minimal current needed to achieve bending is readily computed as a function of beam energy and device geometry. The condition is found imposing that the equilibrium radius lays within the capillary boundaries,  $\rho_0 < \rho_c + r_c$ :

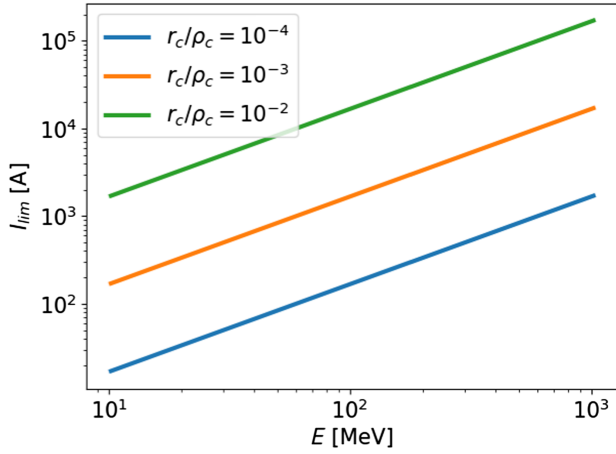


FIG. 3. Minimum required current  $I_{\text{lim}}$  as computed from Eq. (3) as a function of beam energy, for several  $r_c/\rho_c$  ratio values.

$$I > \tilde{I}_0 \gamma \frac{r_c}{\rho_c} = I_{\text{lim}}. \quad (3)$$

Some numerical values of Eq. (3) are shown in Fig. 3. Note that this expression defines the condition for complete charge transport for a pointlike beam, provided that the beam is injected at  $\rho = \rho_0$ . If this last condition is not met, collective oscillations could lead to partial or total charge loss. In general, to transport the beam following non-equilibrium injection, a higher currents will be required.

### B. Equations of motion

In [6], the equations of motion for the curved capillary were identified, assuming that the focusing force is the same of APL. This may be a good approximation for large radii of curvature, but going toward compact devices centripetal force must be taken into account. Referring to Fig. 2(b), the equations of transverse motion will be derived under paraxial approximation with respect to  $(\hat{x}, \hat{y})$  axes, which are centered on the bending plane and on equilibrium radius  $\rho_0$ . The current is assumed to enter the  $(\hat{x}, \hat{y})$  plane. The bending will occur with the center of curvature located at the zero of the horizontal axis  $\hat{\rho}$  and the rotation axis parallel to the  $\hat{y}$  axis. Field component  $\hat{x}$  ( $\hat{y}$ ) will be a linear function of the  $y$  ( $x$ ) coordinate and independent from the  $x$  ( $y$ ) coordinate. They may be written as follows:

$$\begin{aligned} B_x(y) &= -\frac{\partial B}{\partial x} y = B_0 n \frac{y}{\rho_0} \\ B_y(x) &= B_0 + \frac{\partial B}{\partial x} x = B_0 \left( 1 - n \frac{x}{\rho_0} \right), \end{aligned} \quad (4)$$

with  $B_0 \approx \gamma mc/\rho_0 q$  being the field that satisfies the beam rigidity equation and  $n$  being the field index that reads

$$n = -\frac{\rho_0}{B_0} \frac{\partial B}{\partial x} = -\frac{I \rho_0^2}{\tilde{I}_0 \gamma r_c^2}. \quad (5)$$

The difference between the fields in Eq. (4) compared to those of a classical cyclotron is the sign of the  $\hat{x}$  component [11] and leads to the following motion laws:

$$\begin{aligned} x'' + \frac{1-n}{\rho_0^2} x &= \frac{1}{\rho_0} \frac{\Delta \gamma}{\gamma} \\ y'' - \frac{n}{\rho_0^2} y &= 0, \end{aligned} \quad (6)$$

where the prime symbol is now the differentiation with respect to the coordinate  $s$  [see Fig. 2(a)]. A negative field index is always met, ensuring stability in both  $x$  and  $y$  motion. Betatron wavenumbers in both planes are then obtained as follows:

$$\begin{aligned} k_x &= \sqrt{\frac{I}{\tilde{I}_0 \gamma r_c^2} + \frac{1}{\rho_0^2}}, \\ k_y &= \sqrt{\frac{I}{\tilde{I}_0 \gamma r_c^2}}. \end{aligned} \quad (7)$$

Note that, as the radius of  $\rho_c$  goes to infinity,  $k_x \rightarrow k_y \equiv k_b$ , and the obtained expression corresponds to the betatron wave number for an APL as shown in [4,6]. Compared to a CBM wavenumber  $k_x = 1/\rho_0$ , Eq. (7) shows a much shorter betatron wavelength for the ABP, highlighting the intense focusing nature of this device.

### C. Chromatic dispersion

The evolution of a chromatic beam in the ABP shows noticeable differences with respect to a CBM. Given the general expression of dispersion in terms of the wave number  $k_b$  in linear approximation [12]  $D(s) = (1 - \cos k_b s)/\rho_0 k_b^2$ , ABP and CBM dispersions may be written as follows:

$$\begin{aligned} D_{\text{ABP}} &= \frac{1}{\rho_0 k_x^2} (1 - \cos k_b s), \\ D_{\text{CBM}} &= \rho_0 (1 - \cos s/\rho_0). \end{aligned} \quad (8)$$

As an example, for  $\rho_0 = O(1)$  m,  $r_c = O(1)$  mm,  $I = O(1)$  kA, and  $\gamma = O(10^2)$ , the maximum dispersion amplitude is two orders of magnitude smaller than that of a CBM with the same radius of curvature  $\rho_0$ . Such a case is presented in Fig. 4, where the two dispersion function (ABP and CBM) are plotted against longitudinal coordinate ( $s$ ). Moreover, the dispersion vanishes at multiples of the betatron wavelength, which is  $\lambda_x = O(10^{-1})$  m. Including dispersion, the linearized betatron motion becomes

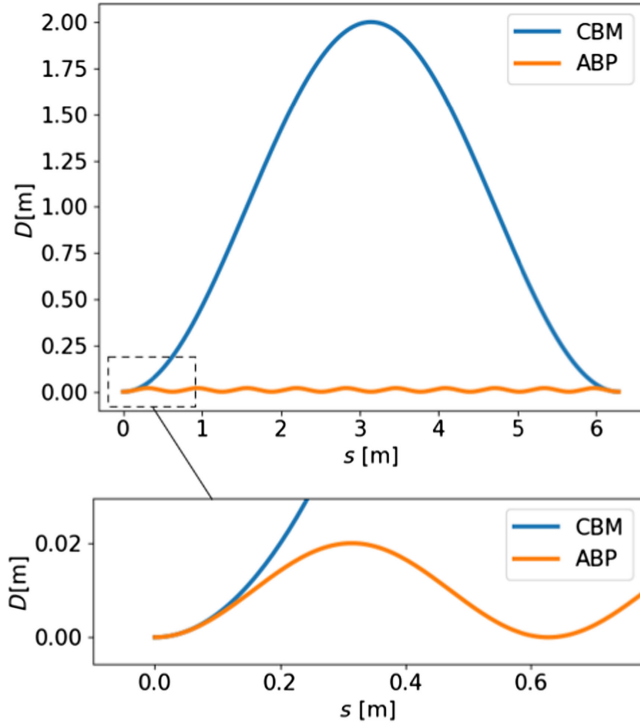


FIG. 4. ABP and CBM dispersion functions comparison, as computed from Eq. (8), for  $\rho_0 = 1$  and  $k_x = 10$ . The dispersion amplitude difference is on the order of  $O(10^2)$ , while the period difference is  $O(10^1)$ . In the detail window below can be observed the same exact trend of the two dispersions for bending lengths  $s \lesssim \lambda_x/4$ : indeed, the ratio between ABP and CBM dispersion is given by a sinc function in Eq. (10) that tends to 1 for  $s \rightarrow 0$ .

$$\begin{aligned} x(s) &= x_\beta(s) + x_D(s) \\ &= \left( x_0 - \frac{\Delta\gamma}{\gamma\rho_0 k_x^2} \right) \cos k_x s + \frac{x'_0}{k_x} \sin k_x s + \frac{\Delta\gamma}{\gamma\rho_0 k_x^2}. \end{aligned} \quad (9)$$

The last term in the RHS of Eq. (9) is the energy-dependent offset with respect to average equilibrium radius  $\rho_0$ , as identified in Eq. (2). Performing the ratio between  $D_{\text{ABP}}$  and  $D_{\text{CBM}}$  in Eq. (8), it is observed that they tend to be the same for small propagation lengths,  $k_x s \ll 1$ :

$$\frac{D_{\text{ABP}}}{D_{\text{CBM}}} = \frac{1}{\rho_0^2 k_x^2} \frac{1 - \cos k_x s}{1 - \cos \frac{s}{\rho_0}} \approx \sin^2 c^2 \frac{k_x s}{2}. \quad (10)$$

The dispersion values start to differ significantly beyond  $s \gtrsim \lambda_x/4$  (where  $D_{\text{ABP}}/D_{\text{CBM}} < 0.8$ ). By approximately inverting Eq. (10), it is possible to obtain the minimum length of the device  $L_c$  as a function of the desired value of  $D_{\text{ABP}}/D_{\text{CBM}}$ :

$$L_c \geq \frac{2}{k_x} \sqrt{6 \left( 1 - \sqrt{\frac{D_{\text{ABP}}}{D_{\text{CBM}}}} \right)}. \quad (11)$$

ABP capillary lengths greater than this limit will give the desired dispersive properties.

#### D. Longitudinal dynamics

As presented in Appendix A, a single particle longitudinal deviation from the reference trajectory ( $\Delta\gamma = 0$ ,  $\rho = \rho_0$ ) is obtained as a function of particle energy and injection conditions. The equation, reported below for convenience, takes the following form:

$$\Delta s \simeq \Delta s_0 - s \frac{a_0^2 k^2}{4} + s \left( \frac{x_0}{2\rho_0} + \frac{1}{\gamma^2} - \frac{\tilde{I}_0 r_c^2 \gamma}{I \rho_0^2} \right) \frac{\Delta\gamma}{\gamma}, \quad (12)$$

with  $s = \beta_\gamma c t$  and  $a_0$  as the betatron oscillation amplitude, defined in Eq. (A2). Transition energy is then identified by imposing  $\Delta s - \Delta s_0 = 0$ :

$$\left( \frac{x_0}{2\rho_0} + \frac{1}{\gamma^2} - \frac{\tilde{I}_0 r_c^2 \gamma}{I \rho_0^2} \right) \frac{\Delta\gamma}{\gamma} = \frac{a_0^2 k^2}{4}. \quad (13)$$

Equation (13) identifies a hyperbolic surface in the phase space  $(a_0, \Delta\gamma/\gamma)$ , which splits regions ahead or behind the reference trajectory [see Fig. 5(a)]. Points with  $\Delta\gamma/\gamma$  below (above) Eq. (13) after (before) the vertical asymptote, will always have  $\Delta s < 0$ , while the others will have  $\Delta s > 0$ : referring to Fig. 5(b), note that the presence of finite emittance (nonzero trajectory angle  $x'$ ) determines a spread of transition hyperbolae (orange in the figure), which partially violates the transition and result in a global beam slowdown. Setting  $x_0 = 0$  in the LHS of Eq. (13), transition Lorentz factor  $\gamma_T$  is found:

$$\gamma_T \simeq \sqrt[3]{\frac{I \rho_0^2}{\tilde{I}_0 r_c^2}} \simeq \sqrt[3]{\frac{I \rho_c^2}{\tilde{I}_0 r_c^2}}, \quad (14)$$

where the second approximation arises from retaining only terms of the same order of magnitude as  $\gamma^3$ . Since the transition Lorentz factor depends on the current, which is lower limited by Eq. (3), a lower limit to the transition Lorentz factor is implied:

$$\gamma_{T,\text{lim}} \simeq \sqrt[3]{\frac{\rho_c \gamma}{r_c}}. \quad (15)$$

Note that this limit depends on the energy of the beam. In particular, Eq. (15) indicates that for beams with  $\gamma > \sqrt{\rho_c/r_c}$ , we will have  $\gamma_{T,\text{lim}} < \gamma$ , meaning it will be possible to place the beam above or below the transition, whereas for beams with  $\gamma < \sqrt{\rho_c/r_c}$ , we will have  $\gamma_{T,\text{lim}} > \gamma$ . In this case, the beam will be bounded below the transition [see Fig. 5(b)]. This could become relevant for ultrashort beam applications (see Sec. II E 1).

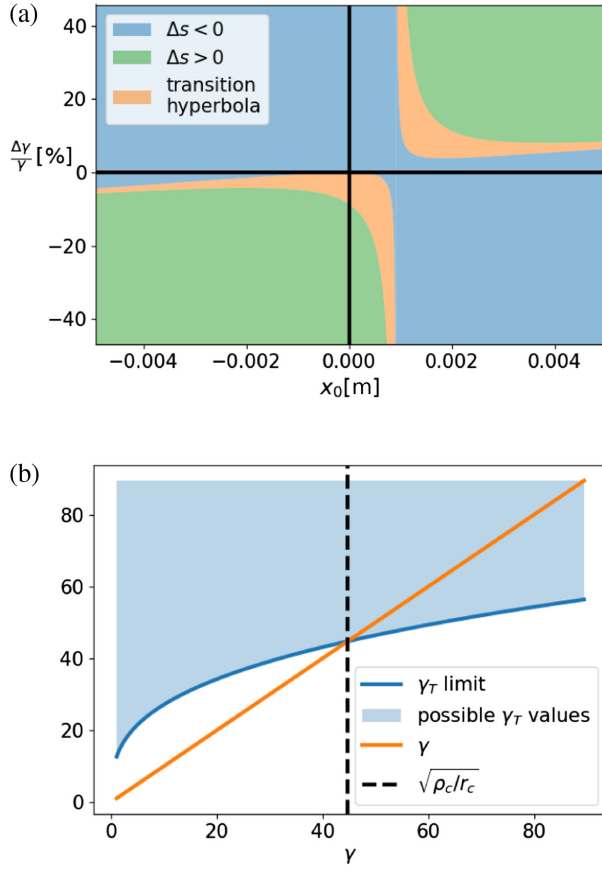


FIG. 5. ABP transition: (a) 1–6 transition space for a whole beam above transition, where regions corresponding to faster (slower) states relative to the reference trajectory are highlighted in green (blue). The presence of finite emittance broadens the transition hyperbola (orange), resulting in an excess of states at  $\Delta s < 0$  (slower beam centroid); (b)  $\gamma_T$  limit, with possible  $\gamma_T$  values as a function of beam energy (abscissa), where it can be observed that for  $\gamma < \sqrt{\rho_c/r_c}$  (dashed black line), the beam will be constrained below the transition.

## E. rms beam parameters

### 1. Transverse

The transverse envelope equation in cylindrical coordinates derivation is reported in Appendix B. For convenience, the final equation is shown below:

$$\frac{\partial^2 \sigma_x}{\langle \rho \rangle^2 \partial \theta^2} - \frac{\langle \rho' \rangle}{\langle \rho \rangle} \frac{\partial \sigma_x}{\langle \rho \rangle \partial \theta} + k_x^2 \sigma_x = \frac{\epsilon_{\text{rms}}^2}{\sigma_x^3}, \quad (16)$$

where  $\langle \rangle$  stands for an average over beam particles. The matched beam size is readily found to be

$$\sigma_{x,M} = \sqrt{\frac{\epsilon_{\text{rms}}}{k_x}}. \quad (17)$$

It is worth noting that this value is valid both for beam injection at equilibrium and for small deviations from it,

until linear approximation for trajectories holds. Note that Eq. (16) shows an adiabatic damping term despite energy conservation, dependent on radial position instead of beam Lorentz factor. This behavior roots to the rotating reference frame that introduces apparent Coriolis force.

## 2. Longitudinal

Performing standard deviation of Eq. (12) under the assumption of an initially Gaussian beam with matched transverse rms size and injected at equilibrium, the longitudinal rms evolution comes as follows:

$$\begin{aligned} \sigma_s^2 = & \sigma_{s,0}^2 + s^2 \left[ \frac{\epsilon_{\text{rms}}}{4\rho_0} \sqrt{\frac{\gamma}{\gamma_T^3}} + \gamma^2 \left( \frac{1}{\gamma^3} - \frac{1}{\gamma_T^3} \right)^2 \right] \sigma_{\Delta\gamma/\gamma}^2 \\ & + s^2 \frac{\epsilon_{\text{rms}}^2 \gamma_T^3}{4\rho_0^2 \gamma} \left( 1 + k_x^4 \rho_0^4 \frac{\gamma^2}{\gamma_T^6} \right). \end{aligned} \quad (18)$$

It was also assumed the bunch to be in a focus at injection, i.e.,  $\epsilon^2 = \sigma_x^2 \sigma_x'^2$ . The presented expression shows that rms elongation is given by a first emittance and energy spread dependent term, and a second one that depends on emittance only. It was found that in many real-case scenarios, these two terms are comparable. The net effect is that the minimal beam elongation is not always found on transition. As shown in Fig. 6, for growing energy, the optimal condition for beam length conservation is found above transition, with a neat behavior-change point dependent on emittance and relative energy spread.

The evolution of the beam centroid with respect to the reference trajectory needs to be derived for retrieving Eq. (18). It turns out to be

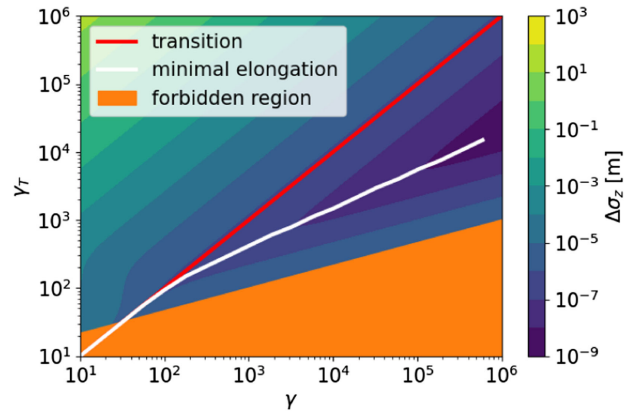


FIG. 6. Beam rms elongation plotted versus beam Lorentz factor  $\gamma$  and transition Lorentz factor  $\gamma_T$  from Eq. (18). Transition line  $\gamma = \gamma_T$  is shown in solid red. Minimal elongation is shown in solid white. The orange region shows out-of-use configurations, where  $I < I_{\text{lim}}$  [see Eq. (3)]. The presented case features  $\sigma_{\Delta\gamma/\gamma} = 0.01$  and  $\epsilon_n = 1$  mm mrad. After some threshold energy given by emittance and energy spread, the optimal condition is found above transition. This knowledge may be relevant in ultrashort beam applications.

$$\mu_s = \mu_{s,0} - s \frac{\epsilon_{\text{rms}}}{2\rho_0} \sqrt{\frac{\gamma_T^3}{\gamma}} \left( 1 + k_x^2 \rho_0^2 \frac{\gamma}{\gamma_T^3} \right) \quad (19)$$

and predicts a global slowdown of the linear beam with the emittance.

### 3. Beam size saturation

Beam energy spread brings equilibrium radius spread. It also leads to a spread in betatron wave vectors, causing a slower or faster phase mixing among the oscillations of beam particles. This phase mixing can have significant effects in cases of off-equilibrium injection and high discharge currents, leading to a considerable increase in transverse size and beam emittance. In Appendix C, the saturation values of the transverse rms size and saturation length as functions of beam and capillary parameters have been derived using a phase-mixing-based statistical approach. For convenience, the final equations for a matched beam are reported below:

$$\sigma_{\text{sat}}^2 = \frac{\Delta x_{\text{inj}}^2}{2} + \frac{\epsilon_{\text{rms}}}{k_x} + \frac{3\sigma_{\Delta\gamma/\gamma}^2}{2\rho_0^2 k_x^4}, \quad (20)$$

$$L_{\text{sat}} \simeq \frac{2\pi\gamma k_x \tilde{I}_0 \rho_0^2 r_c^2}{(I\rho_0^2 - 2\gamma\tilde{I}_0 r_c^2)} \frac{1}{3\sigma_{\Delta\gamma/\gamma}}, \quad (21)$$

where  $\Delta x_{\text{inj}}$  is the injection offset with respect to equilibrium and  $\sigma_{\Delta\gamma/\gamma}$  is the relative energy spread.

### F. Transfer matrix

Combining the results obtained in Secs. II C and II D for a single particle dynamics, in particular Eqs. (9) and (12), linear and nonlinear transfer matrix of the ABP may be obtained, allowing for fast parallel computation of particle trajectories. The nontrivial terms of the linear matrix  $\mathbf{R}_{ij}$  are the following:

$$\begin{aligned} R_{11} &= \cos k_x s, \\ R_{12} &= \frac{1}{k_x} \sin k_x s, \\ R_{16} &= \frac{1}{\rho_0 k_x^2} (1 - \cos k_x s), \\ R_{21} &= -k_x \sin k_x s, \\ R_{22} &= \cos k_x s, \\ R_{26} &= \frac{1}{\rho_0 k_x} \sin k_x s, \\ R_{33} &= \cos k_y s, \\ R_{34} &= \frac{1}{k_y} \sin k_y s, \end{aligned}$$

$$\begin{aligned} R_{43} &= -k_y \sin k_y s, \\ R_{44} &= \cos k_y s, \\ R_{55} &= 1, \\ R_{56} &= s \left( \frac{1}{\gamma^2 - 1} - \frac{\tilde{I}_0 r_c^2 \gamma}{I\rho_0^2} \right), \\ R_{66} &= 1. \end{aligned} \quad (22)$$

Similarly, the nontrivial terms of the nonlinear tensor  $\mathbf{T}_{ijk}$  are the following:

$$\begin{aligned} T_{511} &= -s \frac{k_x^2}{4}, \\ T_{522} &= -\frac{s}{4}, \\ T_{533} &= -s \frac{k_y^2}{4}, \\ T_{544} &= -\frac{s}{4}, \\ T_{516} &= \frac{s}{2\rho_0}. \end{aligned} \quad (23)$$

## III. NUMERICAL SIMULATIONS

Validation of the analytical results derived in Sec. II was performed with a dedicated particle simulation script implemented for the numerical computation of beam dynamics inside the ABP. The related python package is called RADYNO [13]; it computes full relativistic dynamics without space charge and wakefields and optionally performs Lienard-Wiechert-based radiation spectrum evaluation [14]. The beam particles are described relative to the curvature axis of the capillary. This natural coordinate system avoids field interpolation from preconstructed field maps, resulting in good performance. Field is purely magnetic Biot-Savart type. This simplified setup requires constraints on beam aspect ratio and charge [4], which were satisfied for the presented results. Particle trajectory plots will be presented in rectified (cylindrical) coordinates  $(\rho, y, s)$  to clearly observe beam dynamics. In Fig. 7, the injected electron beam has a Gaussian distribution of positions and momenta, mean Lorentz factor  $\gamma = 100$ . The ABP capillary has an inner radius  $r_c = 1$  mm, bending radius  $\rho_c = 15$  cm, and current  $I = 12$  kA. From Eq. (7), the theoretical betatron wavelength can be calculated as  $\lambda_x = 5.3$  cm. In Fig. 7(a), we observe the difference between envelope oscillations due to transverse mismatch (up) and those due to dispersion (down) through rectified trajectory plots. In both cases, the normalized emittance is  $\epsilon_n = 0.1$  mm mrad. In the case of Fig. 7(a) (upper), a beam with  $\sigma_x = 2\sigma_M$  [Eq. (17)] and spread  $\sigma_{\Delta\gamma/\gamma} = 0$  was initialized: optical envelope oscillations at  $\lambda = \lambda_b/2$  are observed, as easily obtained by linearizing the envelope

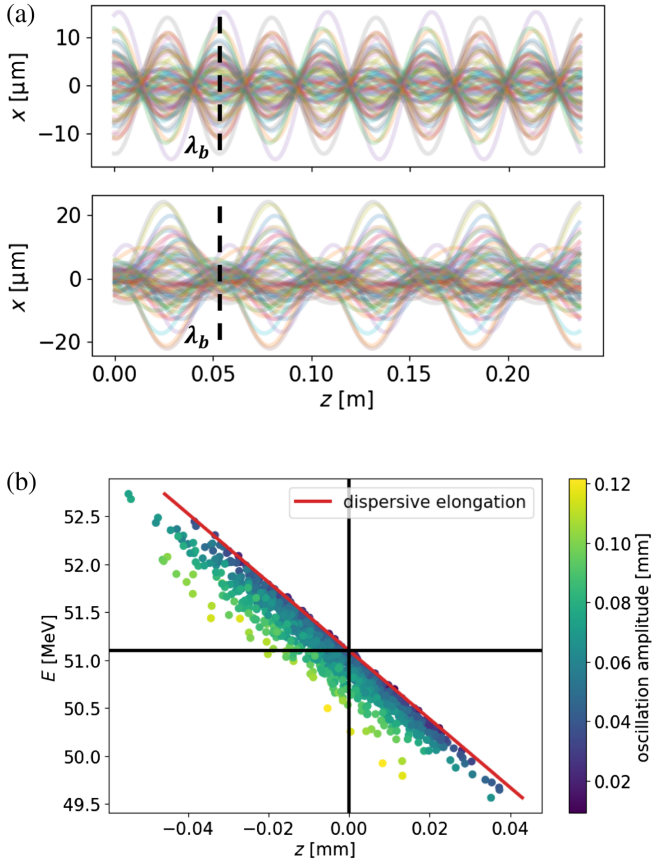


FIG. 7. Transverse and longitudinal beam dynamics. Comparison between numerical and analytical solutions for 50 MeV beams. (a) Numerical rectified trajectories in bending plane, comparison between optical (upper plot, mismatched beam, no energy spread) and dispersive (lower plot, matched beam, 1% energy spread) envelope oscillations. As expected, optical oscillations happen at double frequency compared to dispersive ones. Red dashed line shows expected equilibrium radius Eq. (2). In the dispersive case, note the slight misalignment between oscillation extremes, due to the energy dependence of  $k_x$ ; (b) scatter plot of deviation from the reference trajectory at the end of the evolution of an initially pointlike beam in the longitudinal coordinate and with  $\gamma > \gamma_T$ ,  $\sigma_{\Delta\gamma/\gamma} = 0.01$ , and  $\epsilon_n = 10$  mm mrad. The color bar shows the amplitude of each particle's betatron oscillation, showing a clear correlation with delay respect to reference trajectory.

equation [Eq. (16)]. These oscillations do not alter the emittance. In the case of Fig. 7(a) (lower), a beam with  $\sigma_x = \sigma_M$  and spread  $\sigma_{\Delta\gamma/\gamma} = 1\%$  was initialized: dispersive envelope oscillations at  $\lambda = \lambda_b$ , as indicated by Eq. (8), corresponding to an emittance oscillation, are observed. In particular, this latter case shows that despite the lower dispersion compared to a CBM, the ABP can also provide significant size variations depending on the extraction point. In Fig. 8, beam and capillary parameters are the same used for Fig. 7. In Fig. 8(a), the dispersion of the ABP is quantified in terms of transverse spot size. The ratio between the size of an ABP beam and that of a CBM beam

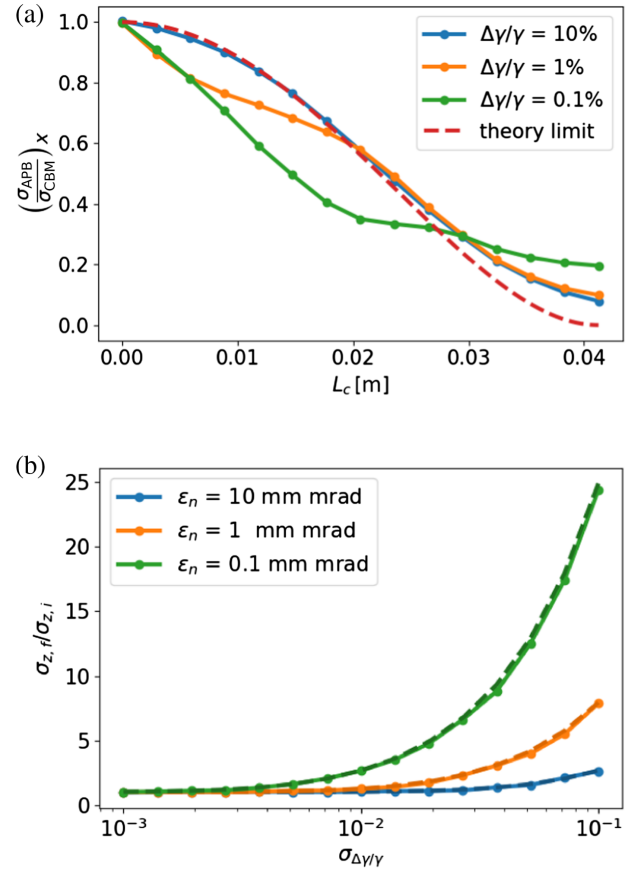


FIG. 8. (a) ABP/CBM transverse spot ratio as a function of device length, evaluated for several  $\sigma_{\Delta\gamma/\gamma}$ . Dashed line shows expected behavior given by Eq. (11), which works properly for greater spot oscillations (e.g., 10% case). (b) Beam rms elongation as a function of energy spread, plotted for matched beams in a wide emittance range. Aspect ratio is set to unity in all cases. Dashed lines are given by Eq. (18) and show good agreement with numerics.

is shown as a function of the device length, for various values of energy spread. The dashed line represents the theoretical trend predicted by Eq. (11), which, being a relationship for a single particle, does not exactly reproduce all cases. Instead, it depicts the behavior for increasing energy spread; this happens because, for lower spreads, we encounter cases where the ABP size variation is smaller than the initial size, making it impossible to verify Eq. (11). Figure 8(a) shows that, in most cases, Eq. (11) can be considered an upper limit of dispersion as a function of device length. In general, the order of magnitude  $L_0 = 2\sqrt{6}/k_x$  can be considered the minimum length beyond which the ABP dispersion is negligible compared to that of a CBM. Figure 8(b), on the other hand, shows the longitudinal dispersive rms variation some emittance values, for an initially matched beam with an aspect ratio = 1. The elongation is evaluated as a function of energy spread, at the end of a  $\pi/2$  bending. The dashed lines represent the analytical predictions given by Eq. (18). It can be observed

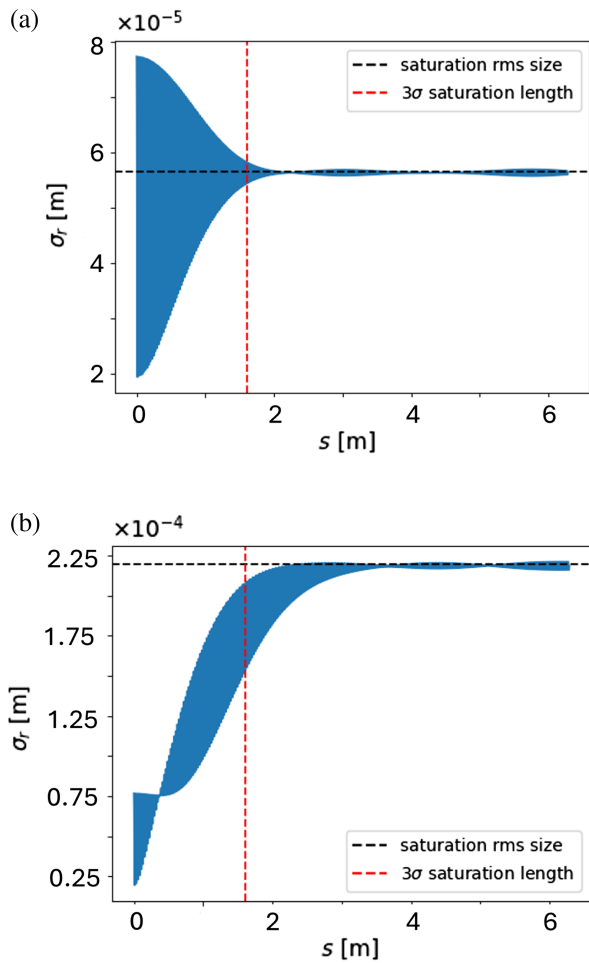


FIG. 9. Transverse rms size saturation with increasing offset with respect to the equilibrium radius  $\Delta x_{\text{inj}} = 0, 0.3$  mm (a), (b). The beam is injected with a double rms size compared to matching, to better observe saturation in case (a). The full blue lines depict the numerical evolution of beam size, while dashed lines represent analytical predictions. The dashed red line indicates the saturation length calculated using Eq. (21), and the dashed black line represents the saturation value from Eq. (C7).

that the elongation is greater for beams with lower emittance, despite Eq. (18) being directly proportional to  $\epsilon_n$ . This occurs because the unitary aspect ratio implies  $\sigma_{z,0} = \sigma_M$ . Also,  $\sigma_M$  is proportional to the emittance and grows more rapidly than Eq. (18), resulting in the observed behavior. Finally, the other relationships derived in Sec. II E, regarding the transverse sizer saturation values and lengths [Eqs. (20) and (21)], were verified. In Fig. 9, the evolutions of  $\sigma_x$  for beams with  $\gamma = 50$ , current  $I = 7500$  A, and  $\sigma_x = 2\sigma_M$  are presented. The choice of these parameters was to reach saturation more rapidly. Injections are performed with offsets  $\Delta x_{\text{inj}} = 0, 0.3$  mm (a), (b). The correct identification of the saturation length can be observed, corresponding to the knee of the average evolution. In case (a), it is less evident due to saturation at a lower value than the maximum, although the correct

identification of saturation remains evident. In both cases, the theoretical saturation value coincides exactly with the numerically calculated one. It is clear how the injection offset does not modify the saturation length while it increases in the transverse size of its same order of magnitude. The treatment presented in Sec. II E is entirely general and proves to be a useful tool for evaluating the progressive degradation of the beam as a function of energy spread, emittance, and injection conditions.

#### IV. CONCLUSIONS

The theoretical work presented provides quantitative insights for the proper preparation of experiments based on ABP devices. The derivation assumes an azimuthal magnetic field of the Biot-Savart type for simplicity. The results are presented in a simple analytical formalism and show excellent agreement with numerical simulations. To include the effects of more realistic magnetic fields [10], it is possible to include a corrective factor to the slope of the linear field as a first approximation. This correction actually modifies the characteristic current  $\tilde{I}_0$  (lower for higher field slopes). Although this still excludes the nonlinearities introduced by current density distribution effects, for matched injection sufficiently close to the capillary axis, the linear approximation will still be accurate. To avoid nonlinear effects, it is advisable in any case to inject the beam as close as possible to the equilibrium indicated by Eq. (2).

One of the most interesting features of the ABP regards its dispersion that can be made orders of magnitude smaller than the one of a CBM with the same curvature radius. On the other hand, it has been shown that the dispersion term actually tends exactly to the one of a CBM for device lengths approaching zero. The dispersion is also inversely proportional to the discharge current, which favors the use of large currents up to the pinching limit [15,16]. However, in Eq. (21), it has been shown that the saturation length of the beam transverse size is also inversely proportional to the current. In case of uncertainty about the injection position, higher currents tend to worsen beam quality more rapidly.

The dispersive properties of the ABP in case of injection out of equilibrium can also be exploited to provide transverse chirp to a beam with substantial energy spread, without having a significant effect on its spot size. The behavior of the beam out of equilibrium is also interesting for the design of ABP chicanes, where the reversal of the bending direction (and therefore the equilibrium position) necessarily leads to collective betatron oscillations of the beam.

#### ACKNOWLEDGMENTS

This work has been partially funded by the European Union—Next Generation EU.

The authors declare no competing interests.

## APPENDIX A: BEAM ELONGATION

Considering a particle in betatron motion around its equilibrium radius, its trajectory can be approximated as

$$r(s) \approx a_0 \cos(ks + \phi_0), \quad (\text{A1})$$

with  $r$  being the radial distance from equilibrium and  $\phi_0$  a phase that we will set to zero without loss of generality; the approximation arises from considering  $k_x \approx k_y \equiv k$ , and

$$a_0 = \sqrt{\left(x_0 - \frac{\Delta\gamma}{\gamma\rho_0 k^2}\right)^2 + \frac{x_0'^2}{k^2} + y_0^2 + \frac{y_0'^2}{k^2}} \quad (\text{A2})$$

is the maximum amplitude of oscillation. Here,  $x_0, y_0, x_0', y_0'$  denote the positions and trajectory slopes of the particle at the time of injection. In paraxial approximation, the axial component of velocity will be

$$\beta_s(s) = \beta_0 \cos[-a_0 k \sin(k_b s)]. \quad (\text{A3})$$

The average longitudinal velocity is found by integrating over half a betatron oscillation as follows:

$$\bar{\beta}_s = \frac{k_b}{\pi} \int_0^{\pi/k_b} \beta_s(s) ds = \beta_0 J_0(k_b a_0) \approx \beta_0 \left(1 - \frac{k_b^2 a_0^2}{4}\right), \quad (\text{A4})$$

where  $J_0$  stands for the Bessel function of the first kind and where

$$\beta_0 = \sqrt{1 - \frac{1}{(\gamma + \Delta\gamma)^2}} \quad (\text{A5})$$

is normalized velocity modulus. The length of trajectory travelled by a particle with Lorentz factor  $\gamma + \Delta\gamma$  in the time interval  $\Delta t$ , averaged over a betatron oscillation, can be expressed as follows:

$$\bar{s}_{\Delta\gamma} = \bar{\beta}_s ct \equiv \left(\rho_0 + \frac{\Delta\gamma}{\gamma\rho_0 k_x^2}\right) \theta_{\Delta\gamma}(t), \quad (\text{A6})$$

where  $\theta_{\Delta\gamma}(t)$  corresponds to the bending angle. The longitudinal position of the particle as a function of time will then be defined as follows:

$$s_{\text{eq},\Delta\gamma} = \rho_0 \theta_{\Delta\gamma}(t) = \frac{\beta_0 \left(1 - \frac{k_b^2 a_0^2}{4}\right)}{1 + \frac{\Delta\gamma}{\gamma\rho_0^2 k^2}} ct. \quad (\text{A7})$$

Expanding Eq. (A7) for  $\Delta\gamma/\gamma \ll 1$ , we obtain the following expression for the longitudinal position:

$$\begin{aligned} s_{\Delta\gamma} &= \frac{\bar{\beta}_s ct}{1 + \Delta\gamma \frac{\tilde{I}_0 r_c^2}{I\rho_0^2}} \approx \beta_\gamma ct \left(1 - \frac{a_0^2 k^2}{4}\right) \\ &+ \beta_\gamma ct \left(\frac{2\tilde{I}_0 r_c^2 \gamma x_0 + I\rho_0 x_0^2 + I\rho_0 y_0^2}{4\tilde{I}_0 r_c^2 \gamma \rho_0}\right) \frac{\Delta\gamma}{\gamma} \\ &+ \beta_\gamma ct \left(\frac{1}{\gamma^2} - \frac{\tilde{I}_0 r_c^2 \gamma}{I\rho_0^2}\right) \left(1 - \frac{a_0^2 k^2}{4}\right) \frac{\Delta\gamma}{\gamma}. \end{aligned} \quad (\text{A8})$$

The zeroth-order term turns out to be nonlinear with the injection amplitude. By retaining only lengths of the same order, it is possible to further approximate Eq. (A8) and express the longitudinal deviation from the reference trajectory as follows:

$$\Delta s \simeq \Delta s_0 - s \frac{a_0^2 k^2}{4} + s \left(\frac{x_0}{2\rho_0} + \frac{1}{\gamma^2} - \frac{\tilde{I}_0 r_c^2 \gamma}{I\rho_0^2}\right) \frac{\Delta\gamma}{\gamma}, \quad (\text{A9})$$

with  $s = \beta_\gamma ct$ .

## APPENDIX B: CURVED ENVELOPE EQUATION

We will define the root-mean-square (rms) radial size and the angular coordinate with respect to the tangent of an instantaneous circular trajectory

$$\sigma_\rho = \sqrt{\langle(\rho - \langle\rho\rangle)^2\rangle}, \quad (\text{B1})$$

$$\rho' = \frac{\partial\rho}{\langle\rho\rangle\partial\theta}, \quad (\text{B2})$$

where  $\langle\rho\rangle$  represents the average radial position of the beam with respect to the axis of curvature of the capillary. The derivative of Eq. (B1) with respect to the average circular trajectory will be

$$\frac{\partial\sigma_\rho}{\langle\rho\rangle\partial\theta} = \frac{1}{\sigma_\rho} \left\langle(\rho - \langle\rho\rangle) \frac{\partial\rho}{\langle\rho\rangle\partial\theta}\right\rangle = \frac{\sigma_{\rho,\rho'}}{\sigma_\rho}, \quad (\text{B3})$$

where  $\sigma_{\rho,\rho'}$  denotes the covariance between  $\rho$  and  $\rho'$ . The second derivative is then obtained as

$$\begin{aligned} \frac{\partial}{\langle\rho\rangle\partial\theta} \left[ \frac{\partial\sigma_\rho}{\langle\rho\rangle\partial\theta} \right] &= \frac{\sigma_\rho^2 \sigma_{\rho'}^2 - \sigma_{\rho,\rho'}^2}{\sigma_\rho^3} + \frac{\langle(\rho - \langle\rho\rangle) \frac{\partial^2\rho}{\langle\rho\rangle^2 \partial\theta^2}\rangle}{\sigma_\rho} - \frac{\langle\rho'\rangle}{\langle\rho\rangle} \frac{\sigma_{\rho,\rho'}}{\sigma_\rho} \\ \frac{\partial}{\langle\rho\rangle\partial\theta} \left[ \frac{\partial\sigma_\rho}{\langle\rho\rangle\partial\theta} \right] &= -\frac{\langle\rho'\rangle}{\langle\rho\rangle} \frac{\partial\sigma_\rho}{\langle\rho\rangle\partial\theta} + \frac{\partial^2\sigma_\rho}{\langle\rho\rangle^2 \partial\theta^2}. \end{aligned} \quad (\text{B4})$$

In the first expression in Eq. (B4), the expression in Eq. (B3) has been differentiated, while in the second expression, the argument within square brackets on the LHS has been differentiated. By equating the two expressions in Eq. (B4), substituting the expression for  $\sigma_{\rho,\rho'}/\sigma_\rho$  from Eq. (B3), and writing the rms emittance as follows:

$$\epsilon_{\text{rms}}^2 = \sigma_\rho^2 \sigma_{\rho'}^2 - \sigma_{\rho, \rho'}^2, \quad (\text{B5})$$

the first and most general form of the envelope equation is obtained as follows:

$$\frac{\partial^2 \sigma_\rho}{\langle \rho \rangle^2 \partial \theta^2} - \frac{\langle (\rho - \langle \rho \rangle) \frac{\partial^2 \rho}{\langle \rho \rangle^2 \partial \theta^2} \rangle}{\sigma_\rho} = \frac{\epsilon_{\text{rms}}^2}{\sigma_\rho^3}. \quad (\text{B6})$$

The paraxial approximation will now be introduced, which is used for the approximate calculation of the acceleration expression. This will allow us to develop the second term on the left-hand side of Eq. (B6). Following the steps indicated in [17], the second derivative of the radial position can be written as follows:

$$\rho'' = -\frac{p'}{p} + \frac{F_r}{\beta c p}. \quad (\text{B7})$$

In the equation above,  $p$  denotes the relativistic momentum of the particle and  $F_r$  represents the radial force acting on it. The first term on the right-hand side (RHS) is zero due to the purely magnetic field, which does not cause energy variations ( $p' = 0$ ). Additionally, the following condition must hold:

$$\rho'' = \frac{\partial}{\langle \rho \rangle \partial \theta} \left[ \frac{\partial \rho}{\langle \rho \rangle \partial \theta} \right] = -\frac{\langle \rho' \rangle}{\langle \rho \rangle} \frac{\partial \rho}{\langle \rho \rangle \partial \theta} + \frac{\partial^2 \rho}{\langle \rho \rangle^2 \partial \theta^2}. \quad (\text{B8})$$

By equating Eqs. (B7) and (B8), we obtain

$$\frac{\partial^2 \rho}{\langle \rho \rangle^2 \partial \theta^2} = \frac{\langle \rho' \rangle}{\langle \rho \rangle} \frac{\partial \rho}{\langle \rho \rangle \partial \theta} + \frac{F_r}{\beta c p}. \quad (\text{B9})$$

We can now proceed with the calculation of the force  $F_r$  acting on the individual particle. It will be given by a component due to the magnetic field generated by the capillary and a centrifugal component given by the cylindrical reference system. For an electron, it will read:

$$F_r = -F_B + F_c = -ec\beta \frac{\mu_0 I}{2\pi r_c^2} (\rho - \rho_c) + \frac{m_e \gamma \beta^2 c^2}{\rho}. \quad (\text{B10})$$

With Eqs. (B8) and (B10), along with Eq. (B3) for replacing  $\sigma_{\rho, \rho'}$ , the second term on the right-hand side of Eq. (B6) can be rewritten as follows:

$$\frac{\langle (\rho - \langle \rho \rangle) \frac{\partial^2 \rho}{\langle \rho \rangle^2 \partial \theta^2} \rangle}{\sigma_\rho} = \frac{\langle \rho' \rangle}{\langle \rho \rangle} \frac{\partial \sigma_\rho}{\langle \rho \rangle \partial \theta} - \left( \frac{\mu_0 e}{2\pi m_e c \beta r_c^2 \gamma} + \frac{1}{\langle \rho \rangle^2} \right) \sigma_\rho. \quad (\text{B11})$$

By substituting Eq. (B11) into Eq. (B6), we obtain the final expression of the envelope equation for the ABP:

$$\frac{\partial^2 \sigma_\rho}{\langle \rho \rangle^2 \partial \theta^2} - \frac{\langle \rho' \rangle}{\langle \rho \rangle} \frac{\partial \sigma_\rho}{\langle \rho \rangle \partial \theta} + \left( \frac{\mu_0 e}{2\pi m_e c \beta r_c^2 \gamma} + \frac{1}{\langle \rho \rangle^2} \right) \sigma_\rho = \frac{\epsilon_{\text{rms}}^2}{\sigma_\rho^3}. \quad (\text{B12})$$

Setting the derivatives with respect to the angular coordinate  $\theta$  and the average centroid velocity  $\langle \rho' \rangle$  to zero (thus assuming  $\langle \rho \rangle = \rho_0$ ), we obtain the matching condition for injection at equilibrium:

$$\sigma_{\rho, M} = \sqrt[4]{\frac{\epsilon_{\text{rms}}^2}{\frac{\mu_0 e}{2\pi m_e c \beta r_c^2 \gamma} + \frac{1}{\rho_0^2}}}. \quad (\text{B13})$$

This expression for the matched rms size also holds for injection outside of equilibrium, as long as the approximation of sinusoidal betatron trajectories remains valid.

### APPENDIX C: TRANSVERSE BEAM SIZE SATURATION

A statistical phase-mixing-based approach will be followed. Let us consider the sinusoidal trajectory of a single particle along the bending plane as  $x(s) = a \cos(ks) + b$ , where  $b$  represents the deviation from  $\rho_0$  due to the particle's energy. Assuming a number  $N$  of betatron oscillations, with  $N$  being an integer,  $N \geq 1$ , the cumulative probability of finding the particle as a function of the distance from  $\rho_0$  is found as follows:

$$P(x) = \begin{cases} 0 & \text{if } x < b - a \\ \frac{1}{\pi} \arccos\left(\frac{x-b}{a}\right) & \text{if } b - a < x < b + a, \\ 1 & \text{if } x > b + a \end{cases} \quad (\text{C1})$$

whose probability distribution function, along with mean and variance, is obtained through differentiation:

$$p(x) = \frac{dP}{dx} = -\frac{1}{\pi a} \frac{1}{\sqrt{1 - \left(\frac{x-b}{a}\right)^2}},$$

$$\mu = b,$$

$$\sigma^2 = \frac{a^2}{2}. \quad (\text{C2})$$

Coefficients  $a$ ,  $b$  depend on energy and initial position:

$$a = \sqrt{\left( \Delta x_{\text{inj}} + \tilde{x}_0 - \frac{\Delta \gamma}{\gamma \rho_0 k_x^2} \right)^2 + \left( \frac{x'_0}{k_x} \right)^2}$$

$$b = \frac{\Delta \gamma}{\gamma \rho_0 k_x^2}, \quad (\text{C3})$$

with  $\Delta x_{\text{inj}}$  representing the injection offset of the beam centroid with respect to  $\rho_0$  and  $\tilde{x}_0$  such that

$x_0 = \Delta x_{\text{inj}} + \tilde{x}_0$ . Assuming independent particles, the total variance may be expressed as the sum of squares:

$$\sigma_{\text{tot}}^2 = \sum_i \sigma_i^2 + \sigma_{\text{eq}}^2, \quad (\text{C4})$$

where the summation over index  $i$  is to be considered over all particles in the beam with  $\sigma$  as in Eq. (C2), and where

$$\sigma_{\text{eq}}^2 = \frac{\sigma_{\Delta\gamma/\gamma}^2}{\rho_0^2 k_x^4} \quad (\text{C5})$$

represents the equilibrium radii spread associated with the percentage energy spread of particles  $\sigma_{\Delta\gamma/\gamma}$ . The summation in Eq. (C4) is better represented by an integral over the position, angle, and energy probability density function (multivariate Gaussian) of the beam particles, with the following result:

$$\sum_i \sigma_i^2 = \frac{1}{2} \left( \Delta x_{\text{inj}}^2 + \sigma_{x_0}^2 + \frac{\sigma_{x'_0}^2}{k_x^2} + \frac{\sigma_{\Delta\gamma/\gamma}^2}{\rho_0^2 k_x^4} \right). \quad (\text{C6})$$

Combining the contribution provided by Eq. (C5), the saturation rms size results in

$$\sigma_{\text{tot}}^2 = \frac{\Delta x_{\text{inj}}^2}{2} + \frac{\sigma_{x_0}^2}{2} + \frac{\sigma_{x'_0}^2}{2k_x^2} + \frac{3\sigma_{\Delta\gamma/\gamma}^2}{2\rho_0^2 k_x^4}. \quad (\text{C7})$$

In the case of matched injection, replacing  $\sigma_{x_0}$  and  $\sigma_{x'_0}$  through Eq. (17) and the relation  $\epsilon_{\text{rms}}^2 = \sigma_{x_0}^2 \sigma_{x'_0}^2$ , Eq. (C7) takes the following form:

$$\sigma_{\text{tot}}^2 = \frac{\Delta x_{\text{inj}}^2}{2} + \frac{\epsilon_{\text{rms}}}{k_x} + \frac{3\sigma_{\Delta\gamma/\gamma}^2}{2\rho_0^2 k_x^4}. \quad (\text{C8})$$

For  $\Delta x_{\text{inj}} = \sigma_{\Delta\gamma/\gamma} = 0$ , Eq. (20) reduces to  $\sigma_{\text{tot}}^2 = \sigma_{x,M}^2$ , confirming the correctness of the treatment in the limit corresponding to the envelope equation [Eq. (16)].

Beam transverse rms size saturation depends on the progressive mixing of betatron phases due to the difference in mean path length and wave vector of the beam particles. The length where the phase mixing is complete will be identified. We are interested in the single particle bending angle associated with integer multiples of complete oscillations, as a function of the deviation from the mean energy:

$$\theta_{m,\Delta\gamma} = m \frac{2\pi}{k_{\Delta\gamma} \rho_{\Delta\gamma}}, \quad (\text{C9})$$

with

$$k_{\Delta\gamma} = \sqrt{\frac{I}{\tilde{I}_0(\gamma + \Delta\gamma)r_c^2} + \frac{1}{\rho_0^2}},$$

$$\rho_{\Delta\gamma} = \rho_0 + \frac{\Delta\gamma}{\gamma\rho_0 k_x^2}. \quad (\text{C10})$$

Evaluating Eq. (C9) for  $m = 1$  and  $\Delta\gamma \rightarrow 0$  to the first order, we obtain

$$\theta_{1,\Delta\gamma} \simeq \frac{2\pi}{k_x \rho_0} + \pi k_x \tilde{I}_0 \rho_0 r_c^2 \frac{I \rho_0^2 - 2\gamma \tilde{I}_0 r_c^2}{(I \rho_0^2 + \gamma \tilde{I}_0 r_c^2)^2} \Delta\gamma. \quad (\text{C11})$$

The slope of  $\theta_{1,\Delta\gamma}$  depends on the sign of the numerator in the second term on the right-hand side of Eq. (C11). Remembering the constraint  $I > I_{\text{lim}}$  and thus substituting the expression given by Eq. (3), the slope of  $\theta_{1,\Delta\gamma}$  is positive when  $\tilde{I}_0 \gamma r_c (\rho_0 - 2r_c) > 0$ . Considering that, in general, the bending radius is (much) larger than the diameter of the capillary, it is possible to assume that for small  $\Delta\gamma/\gamma$ , the angle covered by a single betatron oscillation is monotonically increasing with the particle energy. Approximating the energy extremes to correspond to  $\pm 3\sigma_{\Delta\gamma}$ , phase mixing will be completed when the following condition is met:

$$\theta_{m+1,-3\sigma_{\Delta\gamma}} = \theta_{m,3\sigma_{\Delta\gamma}}. \quad (\text{C12})$$

By satisfying Eq. (C12), beam energy extremes will be exactly phased by  $2\pi$ ; given the monotonicity of the bending angle as a function of energy, particles betatron phases at intermediate energy will be approximately uniformly distributed in the interval  $[0, 2\pi]$ . Beyond this point, the beam will assume a finite and stable rms size. By substituting Eqs. (C9) and (C10) into Eq. (C12), the index  $m^*$  that meets the full mixing is found

$$m^* \simeq \left( \frac{3I\rho_0^2}{I\rho_0^2 + \gamma\tilde{I}_0 r_c^2} - 2 \right)^{-1} \frac{1}{3\sigma_{\Delta\gamma/\gamma}}, \quad (\text{C13})$$

where the approximation arises from the expansion for small energy spreads. As a first check of the validity of Eq. (C13), note that for a percentage energy spread  $\sigma_{\Delta\gamma/\gamma} \rightarrow 0$ ,  $m^* \rightarrow \infty$ : indeed, for zero spread, there are no differences in betatron period, i.e., no phase mixing. The saturation length will then be obtained from Eqs. (C9), (C10), and (C13) as follows:

$$L_{\text{sat}} = m^* \frac{2\pi}{k_{3\sigma_{\Delta\gamma/\gamma}} \rho_{3\sigma_{\Delta\gamma/\gamma}}} \rho_0$$

$$\simeq \frac{2\pi\gamma k_x \tilde{I}_0 \rho_0^2 r_c^2}{(I\rho_0^2 - 2\gamma\tilde{I}_0 r_c^2)} \frac{1}{3\sigma_{\Delta\gamma/\gamma}}. \quad (\text{C14})$$

- [1] Y. Ehrlich, C. Cohen, A. Zigler, J. Krall, P. Sprangle, and E. Esarey, Guiding of high intensity laser pulses in straight and curved plasma channel experiments, *Phys. Rev. Lett.* **77**, 4186 (1996).
- [2] A. Zigler, M. Botton, F. Filippi, Y. Ferber, G. Johansson, O. Pollack, M. P. Anania, F. Bisesto, R. Pompili, M. Ferrario, and E. Dekel, Consolidating multiple femtosecond lasers in coupled curved plasma capillaries, *Appl. Phys. Lett.* **113**, 183505 (2018).
- [3] X. Zhu, B. Li, F. Liu, J. Li, Z. Bi, X. Ge, H. Deng, Z. Zhang, P. Cui, L. Lu, W. Yan, X. Yuan, L. Chen, Q. Cao, Z. Liu, Z. Sheng, M. Chen, and J. Zhang, Experimental demonstration of laser guiding and wakefield acceleration in a curved plasma channel, *Phys. Rev. Lett.* **130**, 215001 (2023).
- [4] J. van Tilborg, S. Steinke, C. Geddes, N. Matlis, B. Shaw, A. Gonsalves, J. Huijts, K. Nakamura, J. Daniels, C. Schroeder, C. Benedetti, E. Esarey, S. Bulanov, N. Bobrova, P. Sasorov, and W. Leemans, Active plasma lensing for relativistic laser-plasma-accelerated electron beams, *Phys. Rev. Lett.* **115**, 184802 (2015).
- [5] R. Pompili, M. Anania, M. Bellaveglia, A. Biagioni, S. Bini, F. Bisesto, E. Brentegani, F. Cardelli, G. Castorina, E. Chiadroni *et al.*, Focusing of high-brightness electron beams with active-plasma lenses, *Phys. Rev. Lett.* **121**, 174801 (2018).
- [6] T. Yang, H. Cheng, Y. Yan, M. Wu, D. Li, Y. Li, Y. Xia, C. Lin, and X. Yan, Designing of active plasma lens for focusing laser-plasma-accelerated pulsed proton beams, *Phys. Rev. Accel. Beams* **24**, 031301 (2021).
- [7] R. Pompili, G. Castorina, M. Ferrario, A. Marocchino, and A. Zigler, Guiding of charged particle beams in curved capillary-discharge waveguides, *AIP Adv.* **8**, 015326 (2018).
- [8] R. Pompili *et al.*, Guiding of charged particle beams in curved plasma-discharge capillaries, *Phys. Rev. Lett.* **132**, 215001 (2024).
- [9] N. Bobrova, A. Esaulov, J.-I. Sakai, P. Sasorov, D. Spence, A. Butler, S. M. Hooker, and S. Bulanov, Simulations of a hydrogen-filled capillary discharge waveguide, *Phys. Rev. E* **65**, 016407 (2001).
- [10] N. A. Bobrova, A. A. Esaulov, J.-I. Sakai, P. V. Sasorov, D. J. Spence, A. Butler, S. M. Hooker, and S. V. Bulanov, Simulations of a hydrogen-filled capillary discharge waveguide, *Phys. Rev. E* **65**, 016407 (2001).
- [11] F. Chautard, Beam dynamics for cyclotrons, CERN, 2006, <http://cds.cern.ch/record/1005052>.
- [12] M. Reiser, *Theory and Design of Charged Particle Beams* (Wiley, Hoboken, NJ, 2008).
- [13] A. Frazzitta, Python Package Index—PyPI, Python Software Foundation, <https://pypi.org/project/radyno/>.
- [14] A. Frazzitta, A. Bacci, A. Carbone, A. Cianchi, A. Curcio, I. Drebot, M. Ferrario, V. Petrillo, M. R. Conti, S. Samsam, L. Serafini, and A. R. Rossi, First simulations for the EuAPS betatron radiation source: A dedicated radiation calculation code, *Instruments* **7**, 52 (2023).
- [15] W. H. Bennett, Self-focusing streams, *Phys. Rev.* **98**, 1584 (1955).
- [16] J. Shiloh, A. Fisher, and N. Rostoker, Z pinch of a gas jet, *Phys. Rev. Lett.* **40**, 515 (1978).
- [17] M. Ferrario, Injection, extraction and matching, CERN Yellow Reports, Vol. **1**: Proceedings of the 2014 CAS-CERN Accelerator School: Plasma Wake Acceleration (2016).